Abrupt pattern transitions in argon ion bombarded swinging Si substrates

Rakhi and Subhendu Sarkar[*]

Surface Modification and Applications Laboratory (SMAL), Department of Physics, Indian Institute of Technology Ropar, Nangal Road, Rupnagar, Punjab 140001, India

(Received 4 August 2022; revised 24 November 2022; accepted 1 December 2022; published 20 December 2022)

We investigated morphology evolution of 500-eV Ar^+ sputtered Si surfaces at an incidence of 67° using an unconventional method of substrate swinging by different azimuthal angles ($\triangle\phi$ from $0^\circ \rightarrow 360^\circ$) and speeds up to 16 rotations per minute (RPM). The samples displayed four different regimes when they were swung azimuthally by different angles at a speed of 1 RPM. Initially, a hierarchical structure (regime 1) comprised of ripples and triangles was obtained which gave way to only ripples (regime 2) at $\triangle\phi = 80^\circ$. A narrow third regime showed a completely flat surface at 100°. Above this angle, only disordered ripples devoid of any triangles were obtained up to 360° (regime 4). This regime also demonstrated drastic changes in orientation of the ripple wave vector at certain angles of $\triangle\phi$. The wavelengths and roughnesses decreased with higher azimuthal angles. Our observations were found to be highly reproducible. Upon swinging the samples for $\triangle\phi = 70^\circ$ at higher speeds resulted in disordered ripple structures with smoother surfaces. Ripples were found to be the most ordered for 1 RPM speed. In contrast to the above, samples rotated continuously for different durations, when compared with a static case, displayed isotropically roughened surfaces. Two-dimensional slope distributions of the morphologies demonstrated formation of asymmetric ripple structures on the surfaces. Our results were explained in the light of linear and nonlinear regimes of sputtering. The crucial role played by dispersive linear terms explained the formation of the hierarchical structures at small swing angles. Once the dispersive effects die down, the ripples change their orientation. The asymmetry in surface structures was explained by the near-surface mass transport phenomenon at oblique azimuthal angles. This study demonstrates the role of this unconventional technique to drive a system towards abrupt morphological transitions not observed otherwise.

DOI: 10.1103/PhysRevB.106.245420

I. INTRODUCTION

Ion beam irradiation (IBI) has proven itself to be a versatile method to yield nanoscale patterns on solid surfaces by energetic ion collision [1]. The shape and size of these periodic height modulations (or nanopatterns) on solid surfaces can be controlled by suitable choice of physical parameters such as incidence ion energy, incident ion angle, ion flux, fluence (irradiation time), etc. [2–5]. The underlying mechanism leading to pattern formation owes its origin to the basic model given by Bradley and Harper [6]. Essentially, it is an outcome of surface instability due to curvature-dependent sputtering and a surface-diffusive smoothening mechanism which reduces surface tension of the irradiated surface and is best represented by the equation

$$\partial_t h = -\nu_x \partial_x^2 h - \nu_y \partial_y^2 h - B\nabla^4 h. \tag{1}$$

Here, ν_x and ν_y are incidence angle-dependent effective surface tension coefficients. B quantifies the relaxation rate due to the surface diffusion. The model successfully predicted that for an ion incidence angle less (greater) than a critical angle θ_c with respect to the surface normal, the ripple wave vector is parallel (perpendicular) to the projection of the ion beam. However, this model cannot explain ripple orientations in directions different from the x and y axes. It also predicts an exponential increase in surface roughness that does not tally with experimental findings. The nonlinear variant of the above equation used to explain ion-induced nonlinear effects can qualitatively explain oblique ripple orientations [7] and is given by

$$\partial_t h = \sum_{i=x,y} \left[-\nu_i\, \partial_i^2 h + \Omega_i \partial_i^2 \partial_x h + \lambda_i^{(1)} (\partial_i h)^2\right] + \sum_{i,j=x,y} \left[-\mathcal{K}_{ij} \partial_i^2 \partial_j^2 h - \lambda_{ij}^{(2)}\, \partial_i^2 (\partial_j h)^2\right]. \tag{2}$$

Here, Ω_i denotes the x- and y-dependent coefficients of dispersive terms that contribute to the Fourier mode velocity in an anisotropic way, λ_i denotes nonlinear effects owing to the nonconservative surface mass redistribution, $\mathcal{K}_{ij}$ signifies ion-induced diffusion, and λ_{ij} denotes surface-transport-related nonlinearities that preserve the total amount of material.

Ion beam patterning has been traditionally done at fixed angles of oblique or normal incidence, thereby creating nanopatterns of ripples and dots, respectively [8–13]. Rotating the sample about its surface normal keeping the incidence angle fixed leads to additional effects not envisaged for fixed sample configurations. Zalar *et al.* demonstrated that following such a procedure increases the resolution in the case of depth profile studies [14]. Bradley *et al.* showed theoretically that the rate at which the surface roughens or smoothens

[*]sarkar@iitrpr.ac.in

during sample rotation and the characteristic length scale of the nanopatterns formed are dependent on the period of rotation [15]. Som and coworkers suggested that the surface roughness decreases for large rotation speeds when Si is bombarded with Ar^+ ions. Moreover, the lateral size and height of the mounds scale progressively with fluence [16]. A study by Frost *et al.* on azimuthally rotating InP surfaces yielded hexagonally ordered nanodots at glancing incidence [17].

On the other hand, researchers have also attempted unconventional methods, mostly aimed towards defect minimization of the nanostructures or for creating nanopatterns having other symmetries. Experiments on Au with two perpendicularly placed Ar^+ ion beams at the azimuth done by Kim *et al.* showed that square-symmetric patterns of nanodots are achievable in the erosive regime [18]. Another experiment based on sequential ion sputtering by the same group demonstrated that nanobeads can be formed using the technique [19]. Studies by the same group also prove that patterning a prerippled surface at azimuthally orthogonal directions leads to enhanced nonlinear effects (e.g., redeposition) as compared to an initially flat surface [20]. An experiment on Si using Ar^+ ions by Keller and Frost further demonstrated that defect densities can be reduced by as large as 40% by a suitable choice of sequential ion beam sputtering [21]. A recent work by Kim *et al.* explored nanopattern formation on graphite substrates by azimuthally swinging the substrates during ion beam sputtering [22]. Their study reported that with the swinging of substrate, composite patterns (wall-like structures) were formed on graphite. These patterns were believed to have formed due to quasi-two-dimensional (quasi-2D) mass flow and shadowing effect, two competing mechanisms which rarely work simultaneously during pattern formation. However, the universality of the effects observed have not been proven on other types of material substrates. The types of patterns formed were to a large extent disordered in terms of their surface topographies and orientations. Moreover, the amorphization process of the grain structures for graphite in the event of ion bombardment is less understood, thereby leading to an incomplete understanding of the phenomenon. It is thus evident from the above studies that several groups are resorting to unconventional methods of ion patterning of surfaces, which invokes new phenomena not achievable using a single fixed beam configuration. In spite of all these efforts, a comprehensive understanding of the physical origins leading to well-ordered patterns of varied geometries and orientations for a particular ion-target combination still remains elusive.

Keeping the above in mind, in this work we have investigated the evolution of nanostructures and their unconventional characteristics on an azimuthally swinging Si surface for different azimuthal angles and rotation speeds. We first looked at a surface under static conditions and then compared it with a rotating surface at varying fluences. The disordered morphology of the rotating samples showed drastic differences with the static one with respect to the ripple formation characteristics. Next, we studied an azimuthally swinging Si surface at identical ion beam parameters but for different values of azimuth. Results show transitions from hierarchical to ripple morphology via an intermediate smoothened (devoid of any nanostructure) surface. Abrupt changes of about 90° in ripple orientations are also observed for specific azimuthal angles above 100°. Four different regimes based on pattern transitions can be identified within the angular variations studied. The drastic shifts in ripple morphologies and their orientations are believed to be an outcome of the linear versus nonlinear effects of sputtering. These effects define the different regimes that we observe in our experiments. Finally, we study the structure formation under similar conditions as above, but for varying rotational speeds. Results indicate better ordering of nanoripples specifically at lower rotation speeds. 2D slope distribution analyses of the sample surfaces exhibit formation of asymmetric structures owing to near-surface 2D mass distributions and curvature-dependent sputtering events for this unconventional mode of ion beam patterning. Shadowing is found to play an important role in the present context. These results enrich our understanding of pattern formation for swinging geometries and pave a way for further applications with these alluring patterns by suitably exploiting the ion beam parameter space.

II. EXPERIMENTAL TECHNIQUES

Commercially available undoped polished Si(100) substrates were cut into pieces of 1×1 cm^2 area and cleaned ultrasonically in ethanol for 20 min. Subsequently, they were rinsed with DI (deionized) water and dried in air. The choice of Si was done considering the fact that the structures formed on such surfaces are better ordered and have been well studied, both theoretically and experimentally, for conventional beam parameter conditions. Hence, results obtained for unconventional situations like the present one would be easy to compare with. Ion beam irradiation (IBI) experiments were carried out at room temperature in a vacuum chamber fitted with a 4-cm broad-beam Kaufman ion source. The vacuum inside the chamber had a base pressure of 2×10^{-7} Torr. Irradiations were done with 500-eV Ar^+ ions at an incidence angle of 67° with respect to the surface normal. Each sample was marked at the back with an arrow indicating the ion incidence direction. This helped to ensure placing the samples identically aligned while doing AFM measurements. The current density used was 13.3 mA/cm^2. The ion fluence was kept constant at a value of 7.5×10^{19} ions/cm^2 (i.e., sputtering time of 15 min) for the majority of the experiments, unless otherwise stated. The sample temperature was found to reach 42 °C ± 1 °C during irradiation experiments. To carry out swinging experiments, the sample holder along with the sample was azimuthally swung by an angle $\Delta\phi$ (i.e., $-\phi \rightarrow +\phi$) as shown in Fig. 1. Here, the sample rotates to and fro in an oscillatory fashion, in contrast to a rotating sample where it always rotates in a particular direction (either clockwise or anticlockwise). An alternating current (ac) servo motor controlled the azimuthal swinging angle and rotational speed [in revolutions per minute (RPM)] of the sample holder.

Irradiation for a static sample was carried out using the conditions detailed above. For continuously rotating samples, irradiations were done for 5, 10, 20, 25, and 30 min at the current density stated above with a constant rotating speed of 1 RPM (i.e., 6°/s). For the swing experiments, samples were irradiated using identical conditions as stated above, but with varying angles of $\Delta\phi$ = 10°, 20°, 30°, 60°, 70°, 80°, 90°, 100°, 110°, 120°,

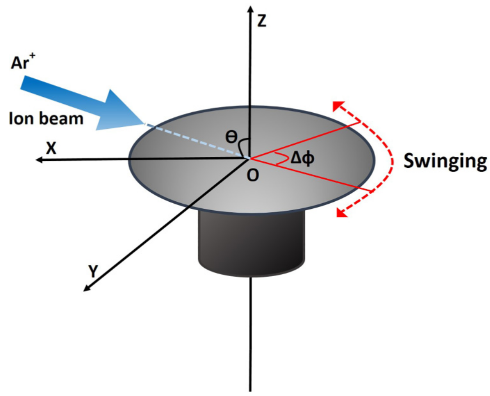

FIG. 1. Schematic view of the swing geometry in azimuth (ϕ) during IBI. θ ($= 67^\circ$) is the polar angle between the 500-eV Ar^+ beam (blue arrow) and the (stationary) surface normal. The sample azimuthally swings for an angle $\triangle\phi$ ($-\phi \rightarrow +\phi$) across the incidence ion beam direction.

180°, 280°, and 360°. A third set of experiments were performed at a fixed $\triangle\phi = 70^\circ$ but with varying rotational speeds of 2, 4, 6, 8, 10, 12 and 16 RPMs. Experiments were repeated to check for reproducibility on several occasions. For all rotation and swing experiments, the rotation and swing and the ion beam were turned on simultaneously.

Post irradiation, the samples were characterized *ex situ* using atomic force microscopy (AFM) (MultiMode 8, Bruker, USA) in tapping mode. The radius of the cantilever used was 10 nm. AFM data were collected from multiple places from the central region of each sample. After obtaining the topographical images of the irradiated surfaces by AFM, quantitative information of the nanostructures were obtained from the acquired data using statistical surface parameters such as wavelength, root-mean-square (rms) roughness (standard deviation of the heights), 2D slope distribution, 2D fast Fourier transform (FFT), and power spectral density (PSD), etc., using Gwyddion (version 8.1) [23]. The one-dimensional (1D) PSDs are estimated in the direction of the ripple wave vector as observed in the AFM images.

III. RESULTS AND DISCUSSIONS

A. Surface morphology evolution of Si surfaces rotating at 1 RPM

We first carried out experiments on rotating substrates and compared their morphology with a nonrotating one. This served as a reference for further swinging experiments. Figure 2 shows 3×3 μm^2 AFM images of Si surfaces irradiated at 500 eV at an ion incident angle of 67° under static and continuously rotating conditions. The static sample was irradiated for 15 min while the rotating ones were irradiated for 5, 10, 20, 25 and 30 min at a speed of 1 RPM as depicted in the figure. The black arrow indicates the initial direction of the incident ion beam on the Si surface. This is considered as the x axis in all our subsequent discussions, unless stated otherwise. For a static sample, this is fixed for the entire period of sputtering. For a rotating or swinging sample, however, the beam is initially aligned in this direction (i.e., at $t = 0$). The top right corners in Fig. 2 show the 2D FFTs while the bottom left corners show 1×1 μm^2 scans corresponding to the AFM images. For the static sample, parallel-mode nanoripples are observed to form on the surface, which are fairly ordered as evident from the satellite peaks of the 2D FFT image [inset of Fig. 2(a)]. The parallel-mode orientation of the ripples is also ascertained from this image. In addition to the ripples, the morphology shows superposed triangular structures which make the morphology a hierarchical one. This observation is commensurate with previous findings in the literature [9,11,25–30]. It turns out that the sputtering yield is not only dependent on the second derivatives of surface heights h but also on their third derivatives $\partial_i^2 \partial_x h$ as discussed in Ref. [31]. Inclusion of this term in the equation of motion (EOM) makes the ripples asymmetric and the ripple propagation dispersive, meaning that the different surface propagating wave vectors (k) travel with different speeds. This dispersive effect can be induced by ion-induced plastic flow or viscous relaxation of ion-induced stresses in the near-surface region. The triangular structure formation at an oblique incidence of the ion beam, theoretically put forward by Bradley and coworkers [26], thus owes its origin to the dispersion terms leading to raised and depressed triangular regions traversed by parallel mode ripples. A highly ordered ripple is formed if both dispersion and transverse smoothening are sufficiently strong. The continuously rotating samples irradiated for different fluences (time durations) show marked distinctions from the static case. The morphology becomes extremely disordered with emergence of fragmented nanoscale structures which show a slight ordering exhibited by the elongated 2D FFT insets. Earlier studies [16,32] have confirmed emergence of similar anisotropic topographies for substrates rotating at very low rotation speeds. This eventually gives way to mounded morphologies as the fluence increases. At higher rotation speeds of 1 RPM, mounded morphologies were obtained in contrast to the current observation. It is worth noting here that the current density in their case [16] was 21.4 $\mu A/cm^2$ which was more than 600 times lower than in the present case (13.3 mA/cm^2). Thus, the two studies indicate that under continuous rotation at high enough fluences slightly anisotropic morphologies can be obtained. The surface roughness and 1D PSD of the irradiated samples are shown in the bottom panel of Fig. 2. For the static sample, the roughness and ripple wavelength are found to be about 5.25 and 44 nm, respectively. When the samples rotate, the roughness decreases and saturates to a value of around 0.6 nm. The absence of any characteristic peak in the PSD spectra for all the rotating samples corroborates to the fact that ripplelike structures are not present in the rotating samples.

An earlier study done by Frost and coworkers [17] on rotating InP surfaces using Ar^+ ions at 500 eV indicates the roughness to scale increasingly with fluence in accordance with early- or late-time regimes. They had observed mounded structures for these surfaces. Similar mounded morphology has also been observed for the case of Si at 0.08 and 1 RPMs [33]. This study also exhibited a saturation of surface roughness at higher fluences. It is to be noted that both these studies were performed at fluences of the order of 10^{15}–10^{18} ions/cm^2. For the present case, the fluence lies between 2.5×10^{19}–15×10^{19} ions/cm^2 corresponding to sputtering

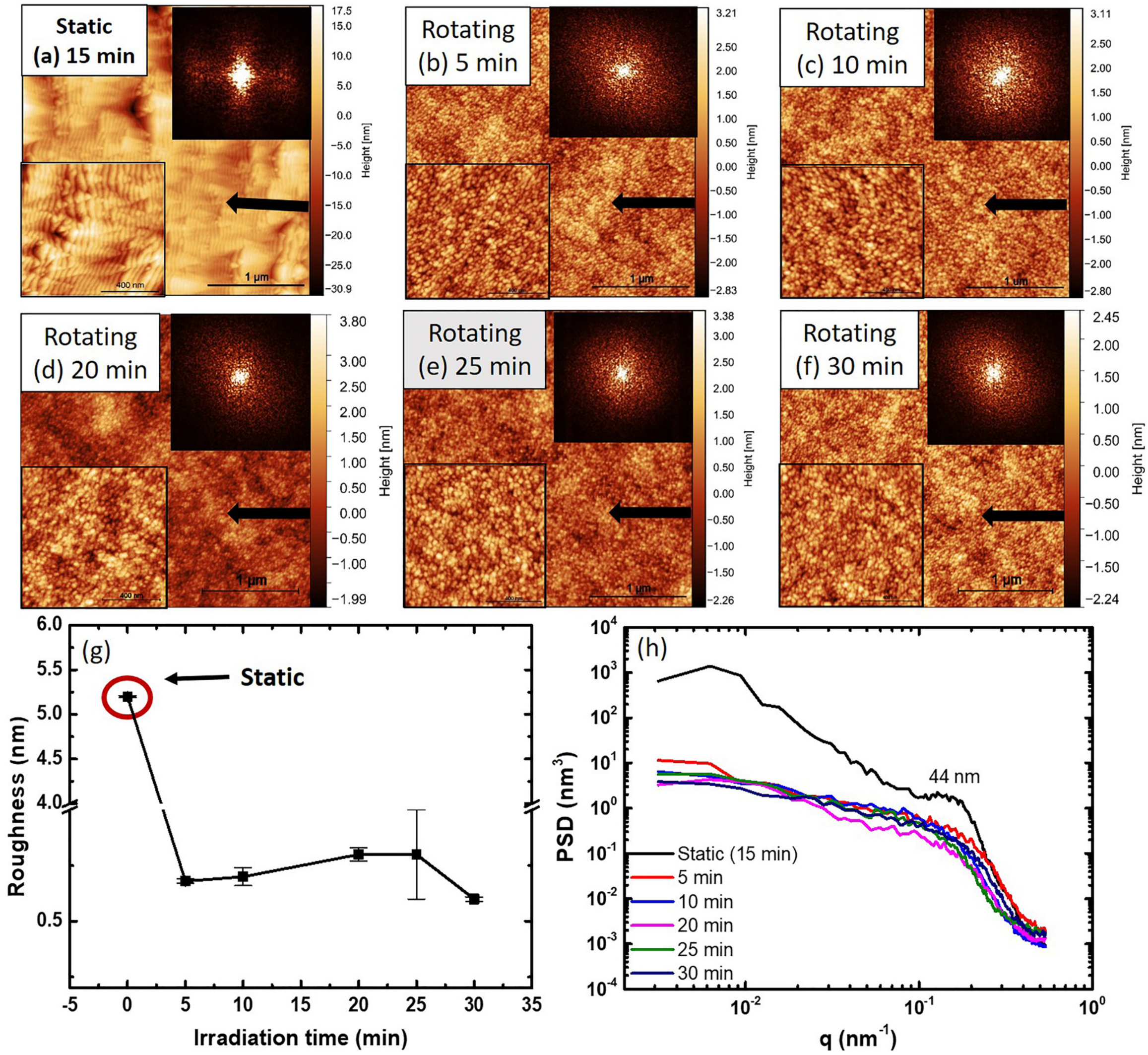

FIG. 2. $3 \times 3\ \mu m^2$ AFM micrographs of 500-eV Ar^+ irradiated Si at 67°. (a) Without rotation with fluence of 7.5×10^{19} ions/cm^2, and for continuous rotation at fluence values of (b) 2.5×10^{19} ions/cm^2, (c) 5×10^{19} ions/cm^2, (d) 10×10^{19} ions/cm^2, (e) 1.2×10^{20} ions/cm^2, and (f) 1.5×10^{20} ions/cm^2, respectively. Black arrow indicates the initial direction of the ion beam prior to rotation. Top right insets: 2D FFTs of corresponding AFM images. Bottom left insets: corresponding $1 \times 1\ \mu m^2$ AFM images. (g) Plot showing rms roughness as a variation of irradiation time. (h) 1D PSD obtained from the AFM images for the irradiated samples. Corresponding $1 \times 1\ \mu m^2$ AFM images provided in Fig. S1 of Supplemental Material [24].

durations of 5–30 min at 500 eV. A recent work by Kim *et al.* using Ar on Si at 2 keV at a speed of 1.12 RPM showed almost no increase of roughness with fluence (1.44×10^{16} ions/cm^2 for their case). The saturation of surface roughness for the present case suggests that the irradiation conditions are in the nonlinear (late-time) regime of sputtering. Moreover, the formation of predominantly disordered structures for all subsequent fluences bear testimony to this fact. The rotating surfaces are also devoid of triangular morphologies, which strongly suggest that dispersive terms (as discussed above) play a nondominant role in the morphology evolution.

B. Surface morphology of irradiated Si surfaces swinging by different azimuthal angles at a speed of 1 RPM

Figure 3 shows $3 \times 3\ \mu m^2$ AFM images of Si surfaces irradiated with increasing values of the azimuthal angle interval ($\triangle\phi$) starting from $\triangle\phi = 0°$ to 360°. For easy reference and subsequent comparison, the Si surface irradiated under static conditions with beam parameters as described in Sec. II is shown. The black arrow in each image signifies the direction of incident ion beam on the Si surface about which the substrate symmetrically swings as shown in Fig. 1. The top right corners in Fig. 3 show the 2D FFTs while the bottom left corners show $1 \times 1\ \mu m^2$ scans corresponding to the AFM images. The orientation of the ripples can be confirmed from the 2D FFT images for the respective irradiated surfaces. The hierarchical morphology obtained for the static sample case ($\triangle\phi = 0°$) has already been described above. Similar hierarchical morphologies are also observed for $\triangle\phi$ angles of 10°, 20°, 30°, 60°, and 70° although with diminishing indication of well-formed triangular structures. For the azimuthal swing angle of $\triangle\phi = 80°$, the triangular morphology is completely absent. The 2D FFT images further suggest that the

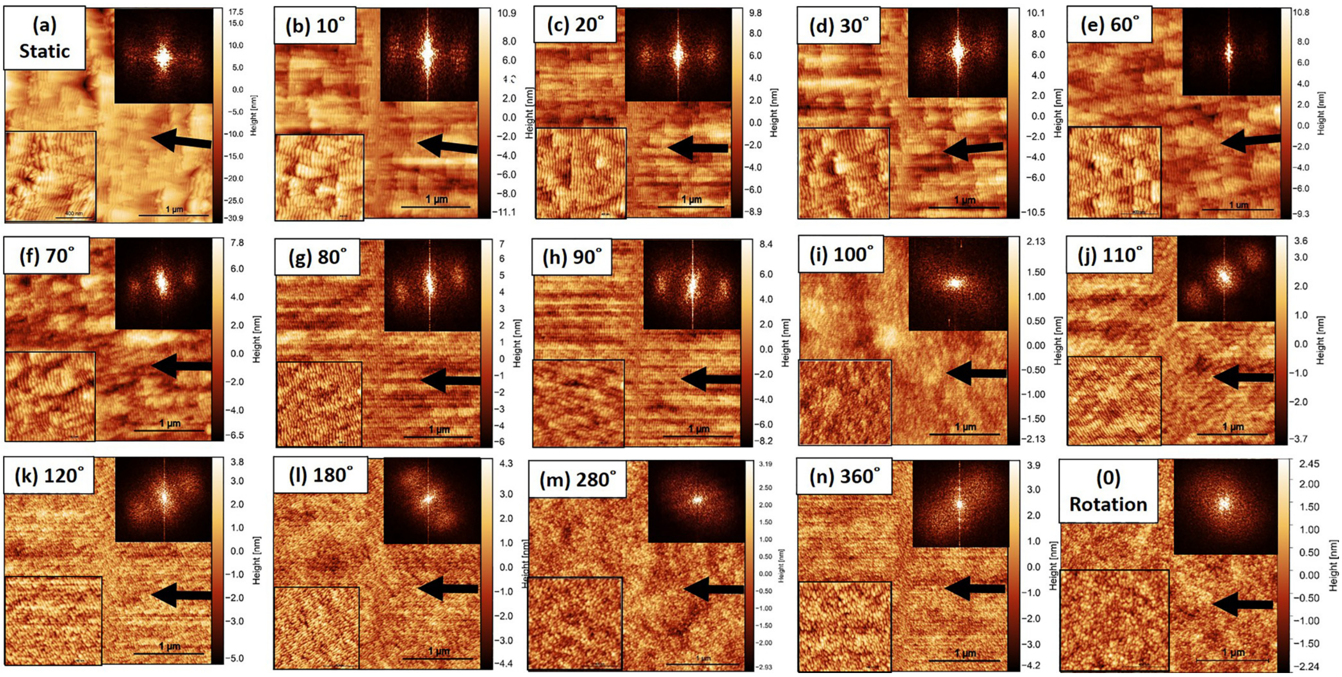

FIG. 3. 3×3 μm^2 AFM micrographs of 500 eV Ar^+ irradiated Si at 67° for different values of swinging angle ($\triangle\phi$): (a) 0°, (b) 10°, (c) 20°, (d) 30°, (e) 60°, (f) 70°, (g) 80°, (h) 90°, (i) 100°, (j) 110°, (k) 120°, (l) 180°, (m) 280°, (n) 360°, and (o) continuous rotation, respectively. Black arrow indicates the initial direction of ion beam prior to rotation. Top right insets: 2D FFTs of corresponding AFM images. Bottom left insets: corresponding 1×1 μm^2 AFM images (also provided in Fig. S2 of [24]).

ripple wave vector is aligned with the starting direction of incident ion beam (x axis as described above) on the Si surface about which the substrate symmetrically swings. Higher swings of azimuthal angles greater than 80° do not show any triangular morphology. Within the experimental conditions, the ripples almost disappear for $\triangle\phi = 90°$. At an angle of 100°, a smooth surface is obtained, devoid of any ripples or triangular morphologies. Furthermore, with increasing swing angle of 110° and 120°, the ripples start to form, but these are oriented at 45° with respect to the x axis. A drastic flip in the ripple orientation by an angle of about $\pi/2$ is observed for a swing angle of 180°. The ripple orientation again flips by $\pi/2$ for a swing angle of 360°. Thus, at higher azimuthally swinging angles, small-scale patterns are observed which are not oriented in either x or y direction. These patterns are oriented approximately at 45° with reference to $+x$ and $-x$ axis. It is to be noted that the ripples formed beyond a swing angle of 100°, in general, shows less ordering as compared to the ripples formed at lower angles of swing (i.e., less than 100°). Thus, within the range of the azimuthal angles studied, a minimum of four regimes can be identified based on the morphological transitions observed. The first regime which shows a hierarchical morphology spans up to $\triangle\phi = 70°$. Beyond this, the second regime exists where only ripples are observed in the absence of triangular structures. The third regime is identified by a flat morphology at $\triangle\phi = 100°$. Beyond this azimuthal angle, there is an onset of the fourth regime which continues until $\triangle\phi = 360°$. During this regime, the irradiated surface is marked by disordered ripple structures. It is to be noted here that the transitions in the ripple orientations have not been taken into consideration during the demarcation of the above regimes.

The evolution of these surface topographies is quantified by evaluating the root-mean-square (rms) roughness, wavelength, and 1D power spectral density (PSD) from the corresponding AFM images (Fig. 4). The rms roughness for the static irradiated sample is about 3.0 nm as evident from Fig. 4(a). It is observed that the roughness decreases drastically as the swing angle increases. The surface has a minimum roughness of about 0.4 nm at a swing angle of 100° where neither ripples nor triangles are observed. As the swing angle is further increased, the roughness increases slightly, essentially saturating to a value of about 0.8 nm. In contrast, the rotating sample has a lower roughness (about 0.7 nm) in comparison to the swinging ones as evident from Fig. 4(a).

The ripple wavelengths were estimated from the peaks of the 1D PSD spectra obtained along the ripple wave vectors from the respective AFM images. The variation of the wavelengths with respect to the swing angle is shown in Fig. 4(b). It is observed that the wavelength is the highest for the static case having a value of about 42.6 nm. With increase in swing angle, this gradually decreases (with some fluctuations) to about 35 nm for $\triangle\phi = 90°$. The wavelength finally saturates to around 28 nm for higher angles of swing. Thus, a sharp drop in ripple wavelength is observed beyond $\triangle\phi = 100°$ at which we observe neither ripples nor triangles (indicated by vertical strips in the figure). The ripple wavelength obtained for continuous rotations of the sample yields a value of 26 nm. Figure 4(c) shows the 1D PSD spectra obtained along

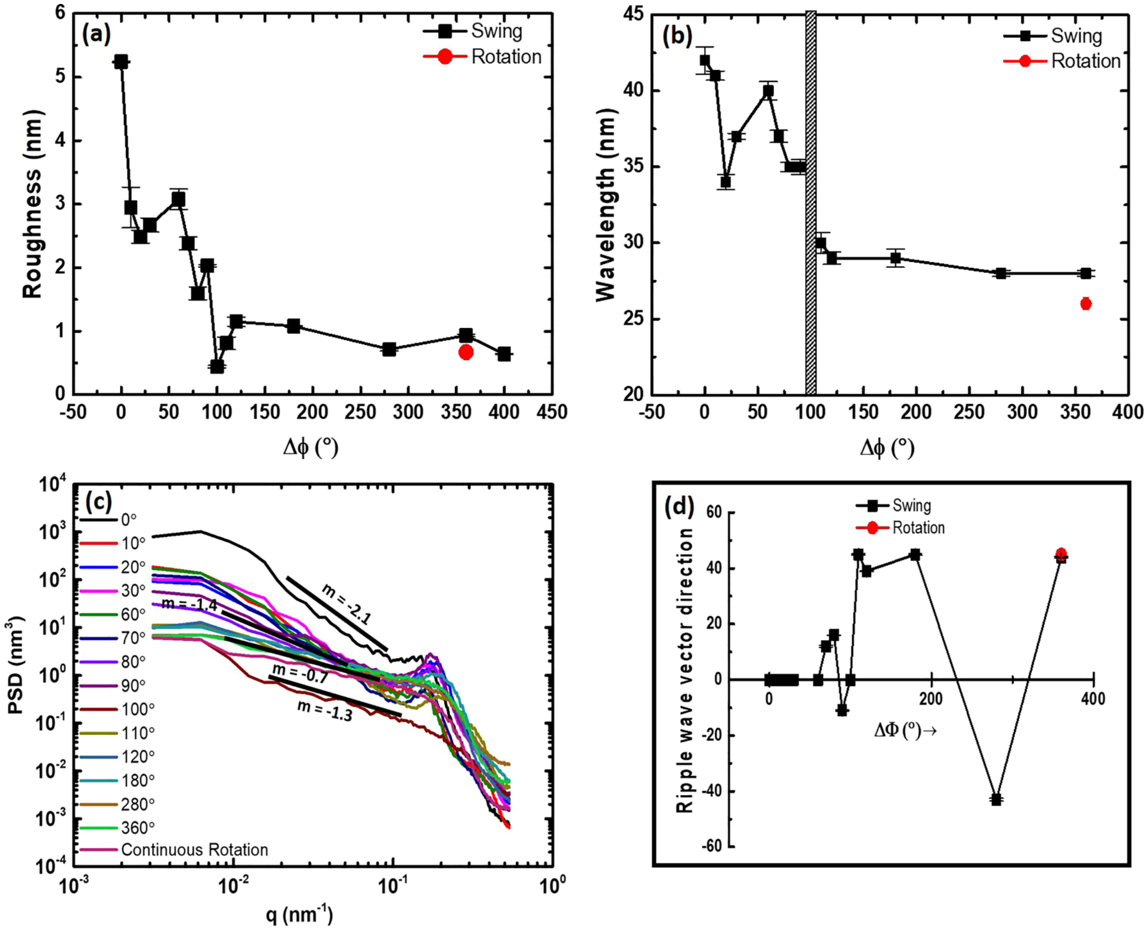

FIG. 4. Plots showing evolution of (a) rms roughness, (b) wavelength, (c) 1D PSD and (d) ripple wave-vector direction for different values of swinging angles such as $\triangle\phi =$ 0°, 10°, 20°, 30°, 60°, 70°, 80°, 90°, 100°, 110°, 120°, 180°, 280°, 360°, and continuous rotation.

the direction of the ripple wave vector for the AFM images shown in Fig. 3. A sharp peak in the PSD spectra usually corresponds to better ripple ordering with fewer defects. The structure factor calculated in the PSD defined as $S(q,t)$ scales as $S(q,t) \sim q^{-m} \sim q^{-(2\alpha+1)}$ under the Family-Vicsek formalism where α is the roughness exponent [8] and $q = 2\pi/l$. For simplicity, Fig. S3 in [24] shows a similar graph with x axis as $q = 1/l$. The PSD spectra are divided into two regimes such as low-q and large-q regimes as shown in Fig. 4(c). At a low-q value, a flat plateau extends out to a critical wave number $q_c = \frac{2\pi}{\lambda_c}$, after which the PSD spectra decrease linearly with a negative slope at a large-q value. The slope m of the curves for low-q values has been calculated from the log-log plots of Fig. 4(c). The corresponding roughness exponents have been subsequently calculated using the values of m. It is observed that the PSD spectra fall into four different categories in terms of their m values. For 0° to 70°, $m = 2.1$ and $\alpha = 0.55$; for 80° to 90°, $m = 1.4$ and $\alpha = 0.2$; for 100°, $m = 1.3$ and $\alpha = 0.15$ for 110° to 360°, $m = 0.7$ and $\alpha = -0.15$. Thus, the surface is rougher at large length scales for lower azimuthal angles below 70°. Beyond this azimuth, the surface displays a smoother morphology at these length scales. Figure S4 in [24] depicts a comparison of 1D PSD plots for an ordered and disordered surface. The ion beam tends to hit the ripple walls more obliquely or even the other side of the ripple walls as we go to higher azimuthal angles. Finally, Fig. 4(d) shows the variation of the ripple wave-vector direction with the azimuthal swing angle.

The different regimes observed as discussed above are surmised to have originated from a chain of events owing to different ion-induced effects. A sharp morphological transition is observed at 100° beyond which hierarchical surfaces and ripples are observed on either sides. As discussed above, the emergence of triangular morphology is necessitated by the dispersion terms in the surface evolution. Nonexistence of the hierarchical morphology thus indicates weakness of these dispersion terms as compared to the transverse smoothening ones. Results imply that as the azimuthal swinging angle is increased, the effect of incidence ion beam angle on dispersion becomes weak and the smoothening effect becomes stronger as compared to the dispersion effect. At a critical swinging angle of $\triangle\phi = 100°$, the smoothening effect overcomes the dispersion effect, thereby rendering the surface a flat featureless morphology. This morphological character bears testimony to the fact that all coefficients of the growth equation have attained stability under such conditions. In a couple of earlier works reported by Madi *et al.* [34,35], they identified stable flat regions between two differently oriented

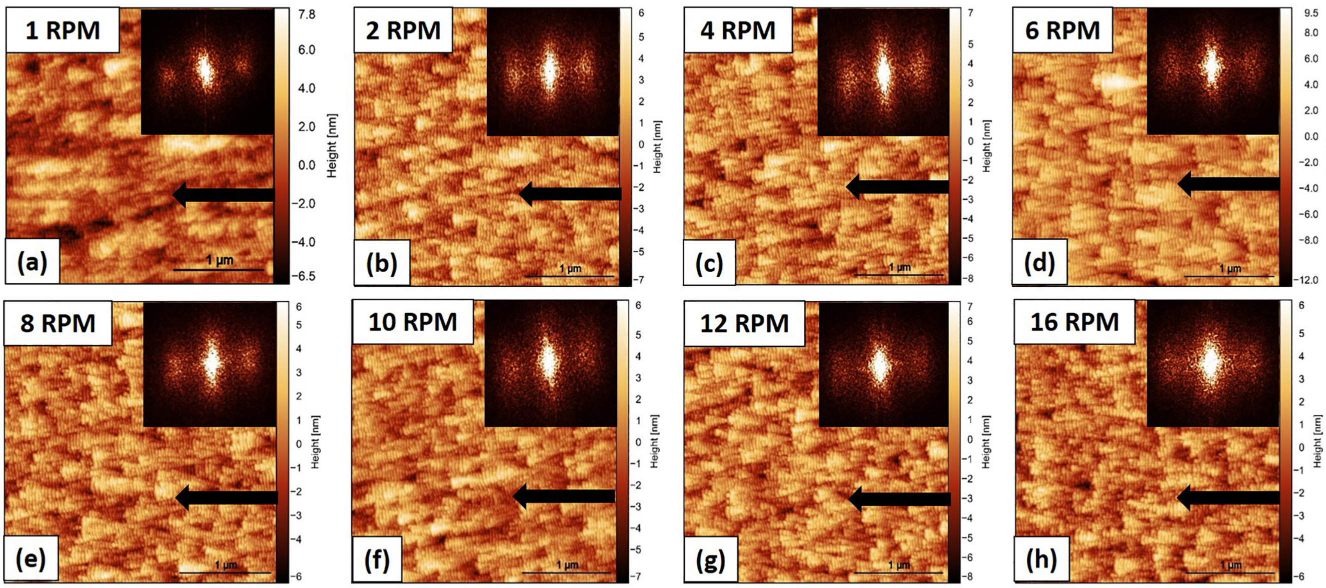

FIG. 5. 3×3 μm^2 AFM micrographs of 500-eV Ar^+ irradiated at $\theta = 67^\circ$ for different rotational speeds (RPM). (a) 1 RPM, (b) 2 RPM, (c) 4 RPM, (d) 6 RPM, (e) 8 RPM, (f) 10 RPM, (g) 12 RPM, and (h) 16 RPM, respectively. Black arrow indicates the initial direction of ion beam prior to rotation. Top right insets: 2D FFTs of corresponding AFM images. Corresponding 1×1 μm^2 AFM images provided in Fig. S5 of [24].

nanostructured regions in the control parameter space of E and θ which was considered to take place via a bifurcation between the pattern-forming and non-pattern-forming regions. In the present context, the control parameter happens to be the azimuthal swing angle (ϕ). The above studies are indicative of the fact that such a bifurcation point may exist in the ϕ parameter space as well. However, establishing this fact necessarily requires an extensive study as done by the previous ones. Above this critical azimuthal angle, the dispersion term diminishes even further, making the surface devoid of any triangular structures. The surface eventually enters the nonlinear regime, as confirmed by the saturation of the rms roughness. The change in orientation of the ripples at 110°, 180°, and 360° is brought about by the phase difference between the ripple wave vector and the direction of the ion beam owing to the swinging of the substrate about the initial position of the substrate, which can leave the system in an unstable mode. In order to incorporate swinging effects the surface evolution equation should depend temporally in a triangular ramp fashion. According to a study [7], Eq. (2) predicts existence of cancellation modes that are height Fourier modes with wave vector in the unstable band for which the nonlinear terms cancel each other. Such a cancellation can leave the system nonlinearly unstable and induce ripple formation. The orientation of ripples, however, would be in an oblique direction, i.e., not parallel to both x or y directions. Further, the surface roughness does not saturate in such a case. For the present situation, however, the surface roughness almost goes towards saturation although not completely as indicated by Fig. S5 in [24]. Therefore, there is a very weak possibility that cancellation mode plays a role in this context. Eventually, with more elapsed time, this effect may die out. Hence, the role of swinging is considered to be of primary importance for the observed effects.

C. Effect of swing speed on surface morphology of irradiated Si surfaces

Consequent to investigating the effect of azimuthal angle on the surface topography of the irradiated Si surfaces, the effect of swing speed was also studied for the same. Figure 5 shows 3×3 μm^2 AFM images of Si surfaces irradiated with 500 eV at a fixed azimuthal angle interval of $\triangle\phi = 70^\circ$ for varying swing speeds. The black arrow indicates the initial direction of the incident ion beam, as stated above. The top right corners in Fig. 5 show the 2D FFTs while the bottom left corners show 1×1 μm^2 scans corresponding to the AFM images. The orientation of the ripples can be confirmed from the 2D FFT images for the respective irradiated surfaces. Hierarchical morphologies consisting of nanoripples and triangles are found for all swing speeds on the irradiated surfaces. The triangular structures are more apparent for speeds of 2 RPM and above. At 1 RPM, they are less ordered and are difficult to notice from AFM images. The 2D FFT images indicate that the ripple wave vectors for all the swing speeds are aligned in similar direction. The satellite peaks of the 2D FFTs also indicate the order of the ripples formed. It is seen that the ripples are best formed at the lowest speed of 1 RPM as confirmed from its narrow satellite peak. As the speed increases, the ripples gradually lose their order and eventually show the least order for 16 RPM within the present experimental domain. The blurriness of the satellite peaks of the 2D FFT (Fig. 5) confirm this fact.

The surface morphologies were better compared and quantified using surface topographical parameters of 1D PSD, surface roughness, and ripple wavelength (Fig. 6). The PSD spectra in Fig. 6(a) show that the peak shifts towards smaller q values as the swing speed increases. The PSD corresponding to a speed of 1 RPM has the sharpest peak thereby asserting that ripples formed under this condition have the best order-

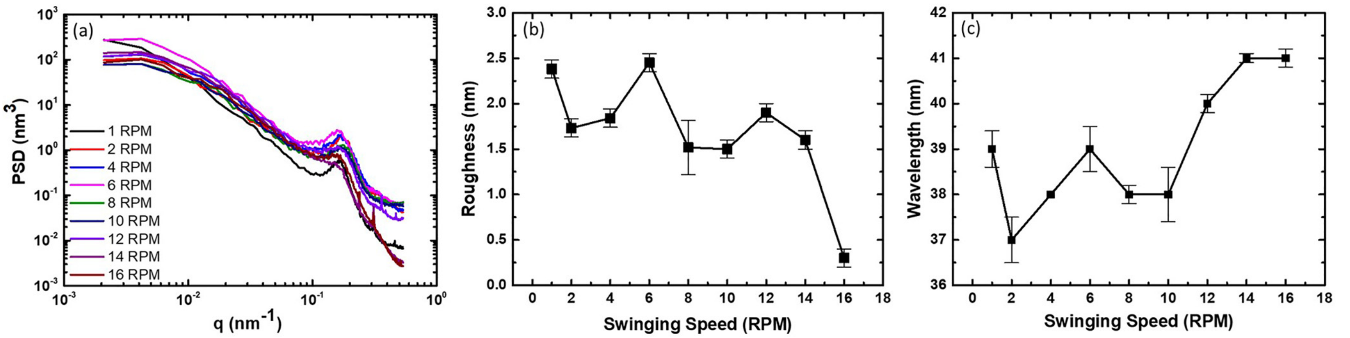

FIG. 6. Plots showing evolution of (a) 1D PSD, (b) rms roughness, and (c) wavelength for different rotational speeds of 1, 2, 4, 6, 8, 10, 12, 14, and 16 RPMs.

ing. The rms roughness plot shows that the roughness of the irradiated surface remains within 1.5 to 2.4 nm up to a speed of 14 RPM (AFM image not shown for brevity). This finally drops to 0.3 nm at 16 RPM. Upon increasing the swing speed, the wavelength of the ripples increases from 37 nm at 2 RPM to a value of 41 nm at 16 RPM. The fluctuations observed in the rms roughness and wavelength values can be attributed to the highly disordered ripples obtained with increase in swinging speeds. The formation of triangles at higher speeds suggests linear dispersion effects to be more dominant at these speeds. It is important to comment here that in contrast to complete rotation at higher speeds where the odd derivatives in the surface evolution equation [Eq. (2)] cancel out [36], all the terms would survive under a swing configuration, thereby making the scenario a nontrivial one. In order to investigate pattern formation at fractional speeds, experiments were carried out at 0.3 and 0.6 RPMs. Figure 7 shows $3 \times 3\ \mu m^2$ AFM images and the corresponding PSDs of the resulting surfaces. The black arrow indicates direction as discussed above. It is clearly observed from the AFM images that ordered nanoripples are formed even at fractional speeds. Ripples are seen to be formed better at 0.6 RPM compared to 0.3 RPM as evident from the less spread of satellite peaks of the 2D FFT inset images. This is further corroborated from the broad PSD peak of 0.3 RPM in comparison to that at 0.6 RPM as found from the 1D PSD plots (Fig. 7) comparing 0.3, 0.6, and 1 RPMs. Out of the above, ripples are probably better formed at 1 RPM as evident from its sharp 1D PSD peak. However, the rms roughness increases as one goes to higher speeds. The slopes at low-k values further indicate that the surface smoothens at large length scales as the rotational speed increases.

D. Effect on local slope distribution

Figure 8 shows the 2D slope distributions obtained from the AFM images (Fig. 3). The shapes of the slope distributions indicate the symmetry or asymmetry of the evolved structures on the irradiated surfaces. It is observed that until a swing angle of about 90°, the distribution predominantly shows a bimodal behavior indicating an asymmetry in the structures. For 100°, a circular distribution is obtained denoting an isotropic surface that corroborates with the flat topography observed in the corresponding AFM image [Fig. 3(i)]. Beyond this azimuth, the distributions indicate an elliptical symmetry arising out of symmetrical nanoripples formed at these angles. The inclinations of the major axes of the 2D slope distributions (about 45°) conform to those of the corresponding FFTs or the ripple wave vector. Finally, for a complete rotation [Fig. 8(o)] the orientation of the distribution flips by an angle of 90°. In contrast to the geometry of complete rotation where each azimuth is bombarded only once per cycle, in the case of swinging it is bombarded twice, thus influencing the curvature-dependent sputtering and other mass redistribution effects in a much more complicated manner.

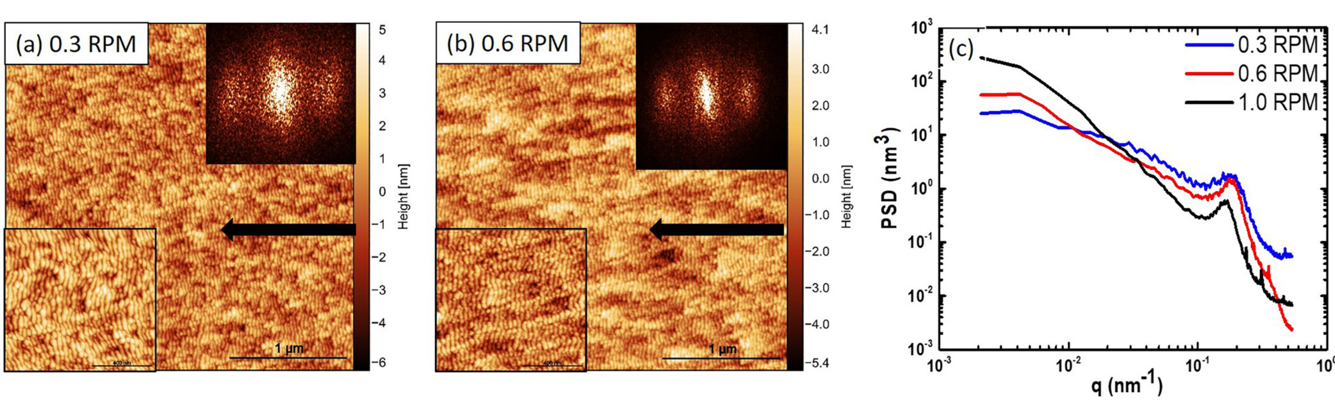

FIG. 7. $3 \times 3\ \mu m^2$ AFM micrographs of 500-eV Ar^+ irradiated Si at $\theta = 67^\circ$ for fractional rotational speeds of (a) 0.3 RPM and (b) 0.6 RPM. Black arrow indicates the initial direction of ion beam prior to rotation. Top right insets: 2D FFTs of corresponding AFM images. Bottom left insets: corresponding $1 \times 1\ \mu m^2$ AFM images. (c) 1D PSD plots for 0.3, 0.6, and 1 RPM obtained from AFM.

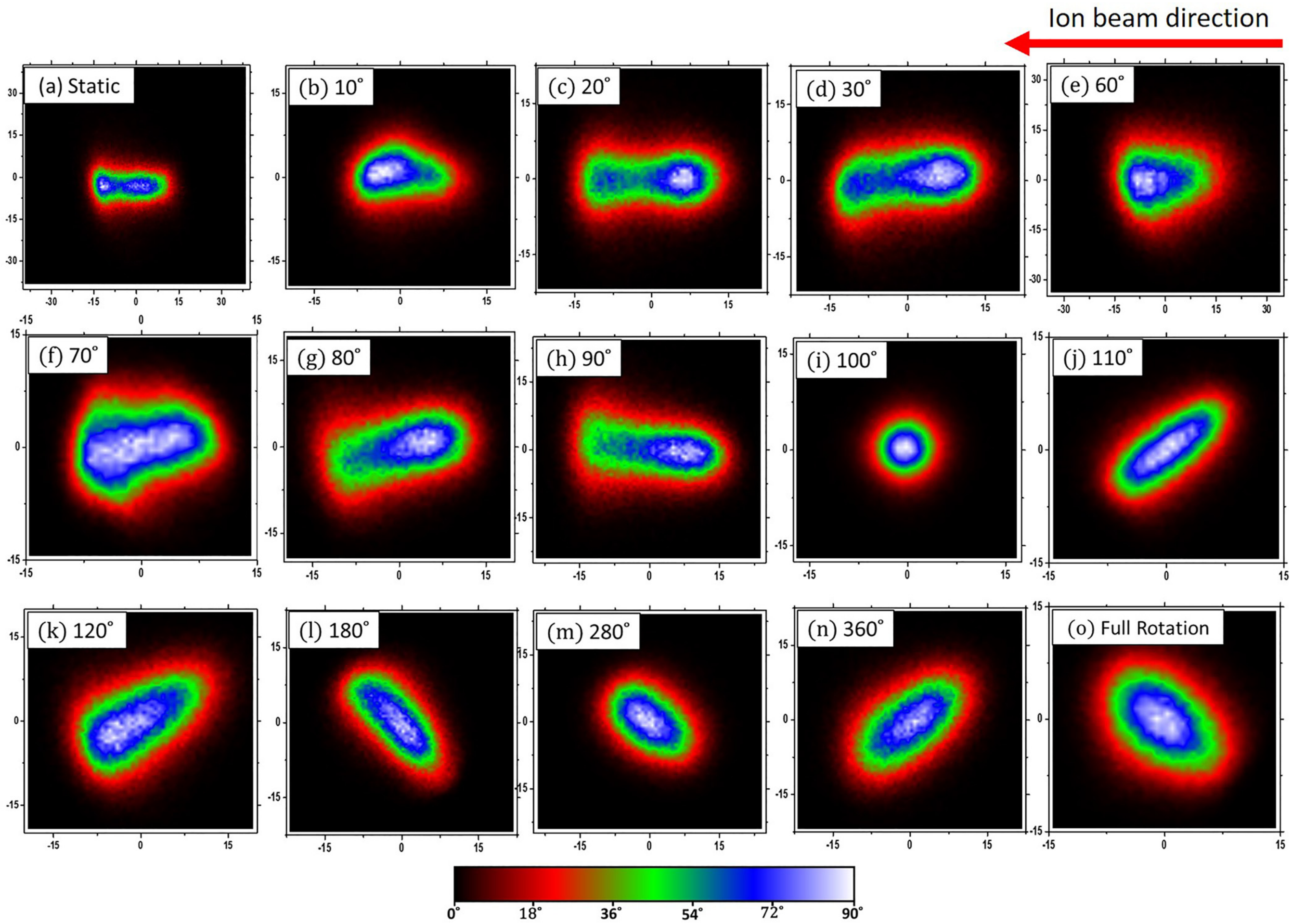

FIG. 8. 2D slope distributions of irradiated surfaces for different azimuthal angles. The horizontal axis is along ion beam direction and vertical axis is perpendicular to the ion beam direction. The red arrow indicates the initial direction of the ion beam prior to swinging.

The above are elucidated through a schematic given in Fig. 9. In this figure, the left panel shows both symmetric and asymmetric AFM images. The middle panel shows line profiles parallel and perpendicular to the ripple wave vector. The right panel shows the corresponding 2D slope distributions and the 1D line profile along the major axis of the slope distribution. For the sake of discussion, the positive x and y directions are considered as depicted in the diagram (left panel). The red arrows indicate direction of the incident ion beam with respect to the polar (incident) angle. The slope of the surface facing the beam is called the front face while the other is termed as the rear face as marked in the image. The slopes are thus positive for the rear face and negative for the front face of ripple patterns. For a symmetric ripple, the slopes on either sides of the peak (i.e., direction parallel to the ripple wave vector) will have similar values except for the opposite (+ve or −ve) signs of $\partial h/\partial x$ [$h(x, y)$ being the surface height]. This can easily be understood from the corresponding 2D slope distribution in the right panel. The 1D line profile along the major axis of the distribution having a single peak reinforces this fact. An asymmetric ripple, on the other hand, exhibits slopes as represented in the bottom row of the middle panel of the diagram. This is well represented in the 2D slope distribution and 1D line profile in the left panel. Existence of more than one peak in the 1D line profile indicates unequal weightages of slope distributions for a surface. Slopes in the y direction (i.e., $\partial h/\partial y$) are evenly distributed for both the types of ripples and will thus have a narrow and symmetric distribution as shown in the middle row of the middle panel. Figure 10 shows the 2D slope distributions obtained from the AFM images (Fig. 5) for different rotational speeds (1 to 16 RPM) for a fixed azimuth of 70°. Based on the above discussion, it is evident from the images that the distribution is asymmetric until 10 RPM, beyond which the asymmetricity reduces to a large extent. For a better insight, line profiles along the ripple wave vectors are extracted from Figs. 8 and 10 and plotted in Fig. 11. It is evident from Fig. 11(a) that up to an azimuthal angle of 90°, the ripples are asymmetric. At 70°, however, the distribution depicts a flat symmetric nature, indicating ripples formed with almost identical slopes on both the front and rear faces. The single narrow symmetric peak at 100° signifies a flat surface as confirmed from its corresponding AFM image. At higher azimuthal angles, the ripples grow in a more symmetric fashion. The asymmetry at lower angles is due to the fact that the beam is initially encountered by the front side of the ripple structures. As the azimuthal angle increases, the ripple slopes are bombarded from oblique (azimuthal) incidences with respect to the normal on the ripple slopes (side walls). This amounts to a large deposition of energy much closer to the surface than for the case of lower

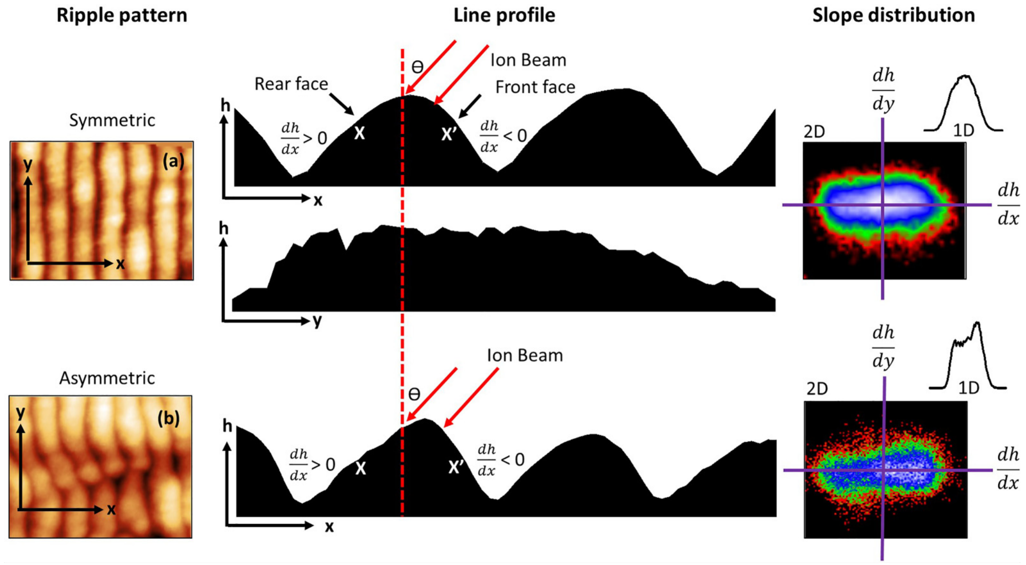

FIG. 9. Schematic demonstrating 2D slope distribution for symmetric and asymmetric nanopatterns. Left panel: representative AFM images showing symmetric and asymmetric ripple patterns. Middle panel: line profiles obtained from AFM images in parallel and perpendicular directions. Red arrows indicate the incident ion beam. Front and rear faces are marked with the signs of their respective slopes. Right panel: 2D slope distributions of the corresponding AFM images. 1D line profiles across the major axis of the distributions are also shown.

or zero azimuthal angles. As a consequence, phenomena like curvature-dependent sputtering and ion-induced surface mass-redistribution effects start playing dominant roles at these conditions. For low azimuthal angles in-depth (bulk) collision cascade events would dominate for a fixed incident (polar) angle. Thus, at higher azimuths, this essentially helps in smoothening of the surface as $\triangle\phi$ increases until at 100° when a flat morphology is obtained. The contribution of the linear dispersion terms towards surface instability becomes weak as evidenced from the loss of triangular structures. Beyond this point, the distribution becomes isotropic as noticed from the figure. Now, keeping $\triangle\phi$ fixed at 70° and increasing the swing

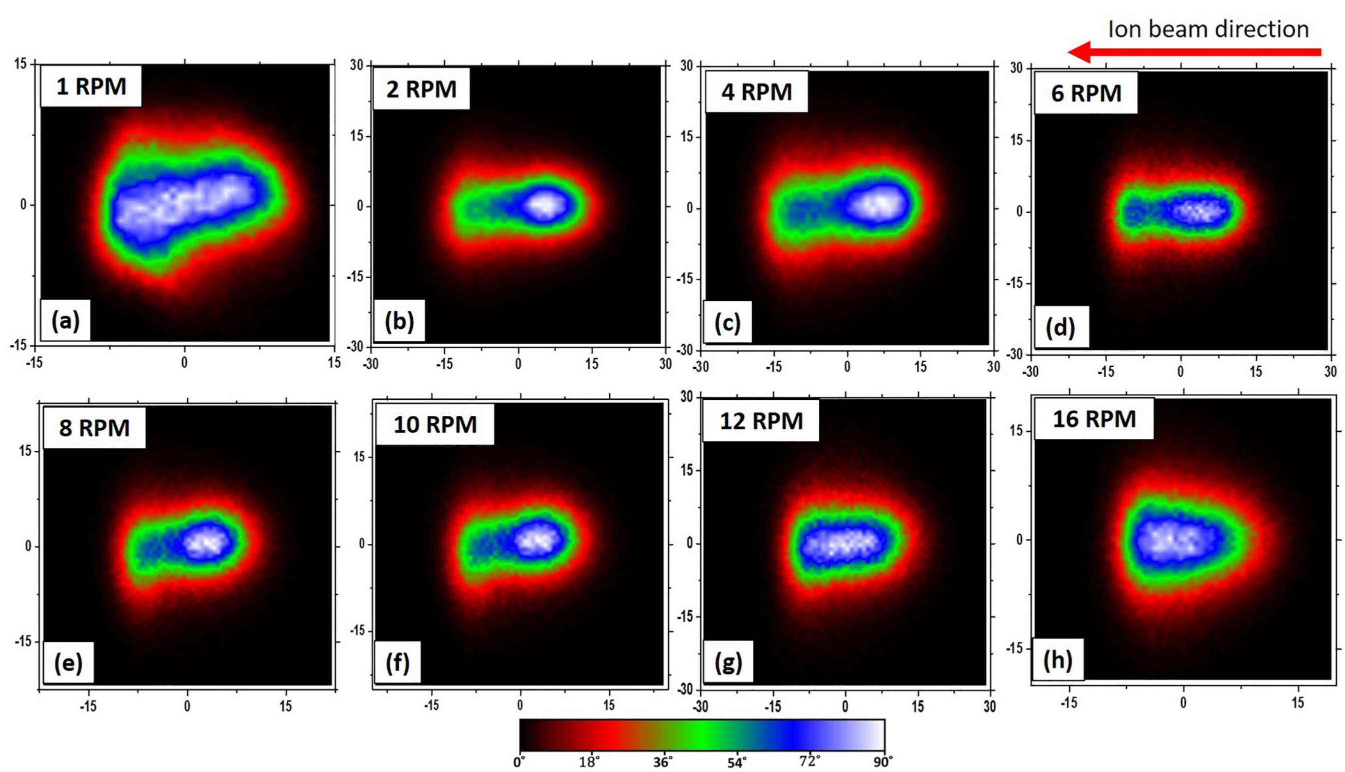

FIG. 10. 2D slope distributions of irradiated surfaces for $\triangle\phi = 70^\circ$ rotating at different rotational speeds. The horizontal axis is along the ion beam direction. The red arrow indicates the initial direction of the ion beam prior to swinging.

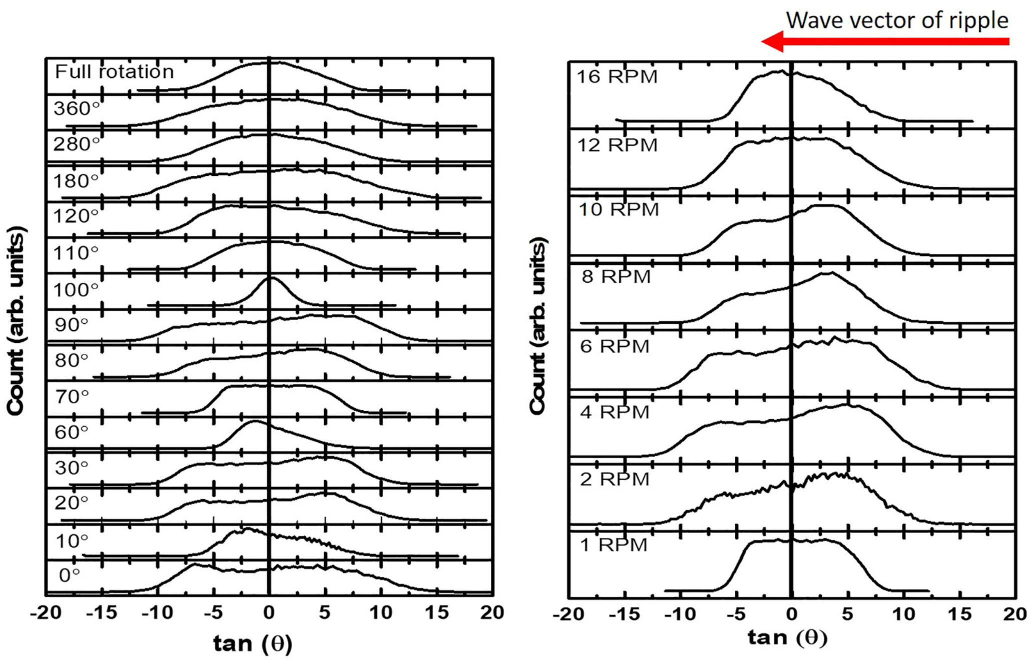

FIG. 11. 1D line profiles obtained along the major axes of the 2D slope distributions for 500-eV Ar^+ irradiated Si surfaces for (a) different swinging angles from 0° to 360° and (b) different rotational speeds from 1 to 16 RPM at $\triangle\phi = 70°$. The red arrow indicates the initial direction of the ion beam prior to swinging.

speeds does not visibly show a change in the AFM images (Fig. 5) but changes the local slopes altogether [as shown in Fig. 11(b)]. For larger speeds, the ripples become asymmetric with the rear faces yielding predominantly smaller slopes as the speed increases. This is clear from the shift of the right-hand peak towards lower values. At large speeds of 12 and 16 RPM, the slopes become more symmetric as seen from the figure. In general, large positive slopes refer to shadowed regions on the surface [37]. However, in the present context, the situation becomes more complicated due to the swinging process. At certain angles, these positive slopes do not produce shadowing whereas other negative sloped regions could induce it. Thus, due to the configuration of the process, the full understanding of these shadowing processes is not obvious.

Most of the earlier studies have reported variations in slope distributions with increase of ion fluence or incident angle [33,38–43]. Bimodal distributions are generally observed at high fluences and incident angles indicating a strong shadowing phenomenon. They also signify transitions between linear and nonlinear regimes of pattern formation. In contrast, this study shows that asymmetric slope distributions can be achieved in an unconventional sputtering scenario even in the absence of a shadowing phenomenon. This is primarily driven by near-surface effects rather than the bulk owing to a higher frequency of bombardment at each azimuth.

IV. CONCLUSIONS

In this study, we performed experiments on Ar^+ irradiated Si surfaces by swinging them through different azimuthal angles at a fixed ion incidence angle of 67°. In addition, surface morphologies were also studied for different swing speeds from 1 RPM up to a maximum of 16 RPM. Based on the nanostructure morphology, four different regimes were observed for different azimuthal angles which included ripples along with triangular structures, ripples devoid of triangles, smooth surfaces, and disordered rippled topographies. In addition, in the last regime of disordered ripple morphology, the orientations of the ripple wave vector exhibited abrupt changes of as large as 45° with respect to the incident ion direction. The PSD spectra clearly corroborated the presence of the above four different regimes stated above. Slope calculations reveal that the surface is rougher at large length scales for lower swing angles. Beyond this, the surface tends to be smoother at these length scales. The ripple wavelength decreased from 42.6 nm for the static surface to 28 nm for the swinging surface while the rms roughness was found to decrease from 3.0 to 0.4 nm, respectively.

For a particular azimuth, the most ordered ripples were formed for the swing speed of 1 RPM as compared with fractional or higher rotational speeds. On comparing static and rotating surfaces, we have illustrated that hierarchical structures are obtained from the former configuration whereas isotropically rough surfaces are obtained for the latter ones. The roughness, however, decreases with fluence or higher rotation speeds. The rms roughness varied from 5.25 to 0.6 nm over this range.

2D and 1D slope distribution calculations were also carried out from the AFM images. They demonstrated presence of asymmetric ripple patterns on Si surface for smaller swing angles primarily owing to the ion-induced near-surface 2D mass distribution. Further, shadowing is found to play a definitive role in deciding the surface topography in this unconventional format of ion irradiation. Our results were explained in the light of dispersive effects of the propagating wave vectors owing to ion-induced surface phenomena. We find that as long as the triangular structures appear owing to the role of dispersive effects, the ripple direction does not change. Once the dispersive effects disappear, the ripples change their orientation. Further, the existence of cancellation modes is believed to have a minimal effect on the ripple characteristics.

We believe our study sheds light on the evolution of pattern formation in unconventional formats of ion sputtering within the present azimuthal regime and swinging speeds. The observed results also indicate lacunae within the current surface evolution models which fail to predict the findings which demonstrate the existence of a plethora of interplaying ion-induced effects capable of driving the system into instabilities, hence giving rise to abrupt transitions. Given that the amorphization process for semiconductors under ion bombardment is better understood than that for graphite (as in Ref. [22]) in addition to the presence of grain boundaries in the latter, the present results can encourage advancement of existing theoretical models for these unconventional geometries. Thus, apart from the possible applications emanating from the intriguing patterns, these results augment a better understanding of this unique IBS format.

ACKNOWLEDGMENTS

The authors would like to thank Professor R. M. Bradley and Professor R. Cuerno for fruitful and enlightening discussions during this work. This work is supported by Department of Science and Technology, Science and Engineering Research Board, India (DST SERB Grant No. SR/S2/CMP-112/2012) and IIT Ropar. The authors also thank H. Singh and CRF, IIT Ropar for help in acquiring AFM data.

[1] *Ion Beam Modification of Solids*, edited by W. Wesch and E. Wendler (Springer, Cham, 2016).
[2] J. Munoz-Garcia, L. Vazquez, M. Castro, R. Gago, A. Redondo-Cubero, A. Moreno-Barrado, and R. Cuerno, Mater. Sci. Eng.: R **86**, 1 (2014).
[3] A. Toma, F. B. de Mongeot, R. Buzio, G. Firpo, S. Bhattacharyya, C. Boragno, and U. Valbusa, Nucl. Instrum. Methods Phys. Res., Sect. B **230**, 551 (2005).
[4] U. Valbusa, C. Boragno, and F. Buatier de Mongeot, J. Phys.: Condens. Matter **14**, 8153 (2002).
[5] Q. Wei, J. Lian, S. Zhu, W. Li, K. Sun, and L. Wang, Chem. Phys. Lett. **452**, 124 (2008).
[6] R. M. Bradley and J. M. Harper, J. Vac. Sci. Technol. A **6**, 2390 (1988).
[7] R. Cuerno, J. Muñoz-García, M. Castro, R. Gago, and L. Vázquez, MRS Online Proc. Libr. **1059**, 1059-KK01-06 (2007).
[8] A. Keller, R. Cuerno, S. Facsko, and W. Möller, Phys. Rev. B **79**, 115437 (2009).
[9] A. Keller and S. Facsko, Materials **3**, 4811 (2010).
[10] B. Ziberi, F. Frost, and B. Rauschenbach, J. Vac. Sci. Technol. A **24**, 1344 (2006).
[11] M. Castro, R. Gago, L. Vázquez, J. Muñoz-García, and R. Cuerno, Phys. Rev. B **86**, 214107 (2012).
[12] R. Cuerno, L. Vázquez, R. Gago, and M. Castro, J. Phys.: Condens. Matter **21**, 220301 (2009).
[13] W. L. Chan and E. Chason, Phys. Rev. B **72**, 165418 (2005).
[14] A. Zalar, Thin Solid Films **124**, 223 (1985).
[15] M. P. Harrison and R. M. Bradley, J. Phys.: Condens. Matter **27**, 295301 (2015).
[16] T. Basu, D. A. Pearson, R. M. Bradley, and T. Som, Appl. Surf. Sci. **379**, 480 (2016).
[17] F. Frost, A. Schindler, and F. Bigl, Phys. Rev. Lett. **85**, 4116 (2000).
[18] M. Joe, C. Choi, B. Kahng, and J.-S. Kim, Appl. Phys. Lett. **91**, 233115 (2007).
[19] M. Joe, J. Kim, C. Choi, B. Kahng, and J. Kim, J. Phys.: Condens. Matter **21**, 224011 (2009).
[20] J.-H. Kim, M. Joe, S.-P. Kim, N.-B. Ha, K.-R. Lee, B. Kahng, and J.-S. Kim, Phys. Rev. B **79**, 205403 (2009).
[21] A. Keller and S. Facsko, Phys. Rev. B **82**, 155444 (2010).
[22] S. M. Yoon and J.-S. Kim, J. Appl. Phys. **119**, 205301 (2016).
[23] http://gwyddion.net/.
[24] See Supplemental Material at http://link.aps.org/supplemental/10.1103/PhysRevB.106.245420 for 1-μm AFM images, PSD plots for ordered and disordered surfaces, and surface roughness evolution.
[25] S. Jo, J. Jun, E. Lee, S. M. Yoon, J. Seo, J. Muñoz-García, R. Cuerno, and J.-S. Kim, Phys. Rev. B **102**, 045421 (2020).
[26] K. M. Loew and R. M. Bradley, Phys. Rev. E **100**, 012801 (2019).
[27] A. Lopez-Cazalilla, D. Chowdhury, A. Ilinov, S. Mondal, P. Barman, S. Bhattacharyya, D. Ghose, F. Djurabekova, K. Nordlund, and S. Norris, J. Appl. Phys. **123**, 235108 (2018).
[28] B. Fares, B. Gautier, P. Holliger, N. Baboux, G. Prudon, and J.-C. Dupuy, Appl. Surf. Sci. **253**, 2662 (2006).
[29] R. Cuerno and J.-S. Kim, J. Appl. Phys. **128**, 180902 (2020).
[30] J. Seo, D. Pearson, R. Bradley, and J. Kim, J. Phys.: Condens. Matter **34**, 265001 (2022).
[31] M. A. Makeev, R. Cuerno, and A.-L. Barabasi, Nucl. Instrum. Methods Phys. Res., Sect. B **197**, 185 (2002).
[32] R. M. Bradley, Phys. Rev. E **54**, 6149 (1996).
[33] D. Datta, S. Garg, T. Basu, B. Satpati, H. Hofsäss, D. Kanjilal, and T. Som, Appl. Surf. Sci. **360**, 131 (2016).
[34] C. S. Madi, B. Davidovitch, H. B. George, S. A. Norris, M. P. Brenner, and M. J. Aziz, Phys. Rev. Lett. **101**, 246102 (2008).
[35] C. S. Madi, H. B. George, and M. J. Aziz, J. Phys.: Condens. Matter **21**, 224010 (2009).
[36] E. Lee, J. Seo, J. Muñoz-García, M. Castro, R. Cuerno, and J.-S. Kim, Phys. Rev. B **105**, 085413 (2022).
[37] G. Carter, J. Appl. Phys. **85**, 455 (1999).
[38] X. Ou and S. Facsko, Nucl. Instrum. Methods Phys. Res., Sect. B **341**, 13 (2014).
[39] R. Dell'Anna, E. Iacob, M. Barozzi, L. Vanzetti, R. Hübner, R. Böttger, D. Giubertoni, and G. Pepponi, J. Phys.: Condens. Matter **30**, 324001 (2018).
[40] M. Kumar, D. Datta, T. Basu, S. Garg, H. Hofsäss, and T. Som, J. Phys.: Condens. Matter **30**, 334001 (2018).
[41] A. Redondo-Cubero, R. Gago, F. J. Palomares, A. Mücklich, M. Vinnichenko, and L. Vázquez, Phys. Rev. B **86**, 085436 (2012).
[42] D. Chowdhury and D. Ghose, J. Phys. D: Appl. Phys. **53**, 335304 (2020).
[43] P. Karmakar, Appl. Surf. Sci. **552**, 149517 (2021).